Modelling challenges of volume-averaged combustion in inert porous media

Pierre-Alexandre Masset, Florent Duchaine, Antoine Pestre, Laurent Selle

Version of Record: https://www.sciencedirect.com/science/article/pii/S0010218023000639
Manuscript_1d51f3ce74e47006d0c798734bc3fb80

Modelling challenges of volume-averaged combustion in inert porous media

P.-A. Masset[a], F. Duchaine[b], A. Pestre[b], L. Selle[a]

[a] *Institut de Mécanique des Fluides de Toulouse, 2 allée du Professeur Camille Soula, Toulouse, 31500, France*
[b] *Centre Européen de Recherche et de Formation Avancée en Calcul Scientifique, 42 avenue Gaspard Coriolis, Toulouse, 31100, France*

Abstract

In porous burners, the flame thickness can be smaller than the pore size, resulting in sharp and locally-anchored flame fronts. The presence of such steep gradients at the pore level is a major hurdle for the derivation of volume-averaged models, particularly for the highly non-linear reaction rates. With the intent to address the difficulties associated with volume-averaging for porous media combustion, this work makes use of 3D Pore-Level Direct Numerical Simulations including conjugate heat transfer and complex chemistry in burners of finite length. These detailed 3D simulations are compared to their 1D volume-averaged counterpart, with effective properties estimated directly on the computational domains and of identical thermochemical scheme. Discrepancies in terms of burning rate, profiles, and *a priori* analysis on the reaction rates are discussed. Various pore sizes and geometries are considered. At the pore level, it is shown that preheating, wrinkling and wall quenching are the three main factors driving the global burning rate. Importantly, hydrodynamic dispersion is shown to have an indirect role on combustion processes. From the observations of combustion at pore scale, a new closure for reaction rates based on a flamelet assumption is proposed. It accounts for flame wrinkling and eliminates the unwanted effect of hydrodynamic dispersion on burning rate.

Keywords: porous media combustion, volume-averaged model, closure model, flame wrinkling, dispersion

1. Introduction

The combustion of a gaseous mixture in an inert solid matrix, referred to as Porous Media Combustion (PMC), is known to increase consumption rates and broaden flammability limits. On the lean side, it enables a substantial reduction in CO and NOx emissions [1]. The main mechanism underpinning this performance is an upstream recirculation of enthalpy from the burnt to the fresh gases through the solid matrix, which enhances combustion kinetics [2]. Though the general principles of PMC and main trends are well understood, the derivation of modelling strategies for the design of industrial burners is still an active field of research. The most popular framework for the numerical simulation of large-scale systems is the Volume-Averaged Model (VAM). The strongly inhomogeneous, non-linear and co-dependent phenomena such as convection, diffusion, conjugate heat transfer, chemical reactions and radiation are all modelled to some extent using VAM, but they show inconsistent agreement with experiments. As recognized by many authors [3–6], this is mainly due to the incomplete knowledge of combustion processes at pore level, which drives the recent experimental and numerical efforts dedicated to characterize PMC at this scale. One of the main open questions is the structure and modelling of the reaction zone embedded in the solid matrix.

On the experimental side, the opacity of the solid makes non-intrusive diagnostics of the internal flame structure notoriously difficult. 1/2D methods such as coherent anti-Stokes Raman scattering [7, 8] or laser-induced fluorescence [9] were attempted, but these require the creation of an artificial/intrusive small gap in the solid matrix or very large pores for optical access. Interestingly, the presence of local temperature maxima along the burner direction was reported in [8], suggesting the existence of non-planar flame fronts. A fairly direct measurement method was proposed by Dunnmon et al. [5] who used krypton as a gaseous adjuvant to reconstruct 3D fields related to the temperature via X-ray tomography. Although the method still suffers from large uncertainties, it could be also assessed that the combustion front is largely non-planar and distributed among the pores. More recently, Fursenko et al. [6] sandwiched a 2D packing of spheres between two quartz plates to visualize directly the oscillatory nature of the flame under filtration combustion. Again, sharp and distorted fronts were observed in the voids. Those experimental strategies, although imperfect, remain more promising that the more classical, 0D and intrusive diagnostic using thermo-

couples inserted within the porous voids [10, 11], which have a tendency to filter out short-scale variations due to strong radiation, physical extension of the probes and spurious contact with the solid matrix.

On the numerical side, some Direct Pore-Level Simulations (DPLS) have been performed to study the internal structure of PMC. Those are summarized chronologically in Tab. 1, where the use of complex kinetics, radiation, mesh resolution and domain sizes are reported for comparison. In 2D, Sahraoui and Kaviany [3] were the first to propose DPLS in regular arrangements of square rods, followed by more recent works [12–15]. These studies reported non-planar flame fronts, and some discrepancies between volume-averaged models and simulations were underlined in [3]. However, a realistic simulation of intra and interphase heat transfers requires the third dimension of space. In 3D, Bedoya et al. [16] presented a joint study of cylindrical and conical burners, in order to compare 1D VAM, 3D DPLS and experiments. Because of differences in the modelling assumptions, no conclusions on the validity of the volume-averaged model itself could be given. Billerot et al. [17] presented the first reacting simulations in regular diamond-based lattices, and reported large pore-scale inhomogeneities. Yakovlev and Zambalov [18] computed unsteady filtration combustion in a packed bed of spheres, showing good qualitative agreement for temperature profiles against experiments. Shi et al. [19] followed through with a similar study, and compared the results to a volume-averaged model. Good agreement was observed, but since the transient displacement speed of the front in filtration combustion mode is mostly governed by a global energy budget [20], these results are less sensitive to the modelling of the reaction rates. Recently, Yakovlev et al. [21] presented simulations of a thin-layered radial burner and found large, finger-shaped flame fronts within the porous matrix. From Tab. 1, several modelling trends can be pointed out. First, the spatial resolution is sometimes rather loose in order to cope with the computational cost on large domains. This may be an issue for the accurate representation of the flame fronts. Also, single-step kinetics dominate the literature, which may hinder the accuracy of the response to preheating [22]. Last but not least, radiation has been increasingly included in the microscopic models. However, whilst it is undeniably an important mode of heat transfer affecting the large scales and consequently the burner operating range [23], its influence on the flame front at the pore level is negligible.

In the works reported above and more generally in the vast majority of the literature on PMC, pore sizes are typically larger than the flame thick-

ness, giving rise to sharp, locally-anchored flame fronts, very similar to the ones classically found in the wake of bluff bodies or injectors. This may have important consequences regarding VAM. First, this observation is a blatant violation of the length-scale separation between micro and macro-scale gradients required for upscaling procedures [24]. Then, there is the implicit assumption that the flame front is locally planar, though both experiments and pore-scale simulations suggest otherwise. Additionally, VAM usually oversee the response of flame fronts to stretch, curvature, non-homogeneous preheating or near-wall quenching taking place in the interstitial flow at the pore level. Finally, though some classical assumptions of VAM for PMC are well documented, such as a interphase heat exchange, or the existence of an effective solid conductivity, the role of hydrodynamic dispersion within PMC remains unsettled. Although dispersion undeniably occurs within porous burners, its macroscale modelling through an increase in diffusivities yields a flame acceleration in the VAM, which has not yet been linked to the pore-scale combustion processes.

Fundamentally, these points are related to the commutation errors between the averaging procedure and the pointwise operators, suggesting an analogy with the modelling issues encountered in turbulent combustion. Consequently, an appropriate closure for the strongly non-linear reaction rates seems in order to retrieve the global burning rate. Unfortunately, to the authors' knowledge such closure model has not yet been proposed for PMC.

By means of 3D DPLS and associated VAM simulations for various pore sizes and geometries, this paper addresses the modelling difficulties of volume-averaging for porous media combustion - when the pore size is larger than the flame thickness and for steady-state conditions. It is shown that, even when the VAM is fed with effective parameters estimated directly on the simulated domains, large errors regarding VAM predictions for flame acceleration and spatially-averaged profiles are observed. The factors driving burning rate locally, such as flame surface density, preheating, wall quenching and stretch are investigated. Eventually, based upon a flamelet approach at pore scale, this study leads to the formulation of a new macroscale model for reaction rates.

The paper is organised as follows. In Sec. 2 the 3D DPLS are presented, as well as the corresponding VAM. In Sec. 3, the effective properties fed in the VAM are computed, and the pore-level structure of the submerged flames is described. In Sec. 4, the relationships between the DPLS and the VAM are investigated - notably in the perspective micro *vs.* macroscale burning

rate. Eventually, Sec. 5 presents an attempt at closing the gap between the DPLS and the VAM through a closure model for reaction rates based on the observations from the DPLS.

2. Microscopic and macroscopic models

2.1. 3D Direct Pore-Resolved Simulations

2.1.1. Computational domains

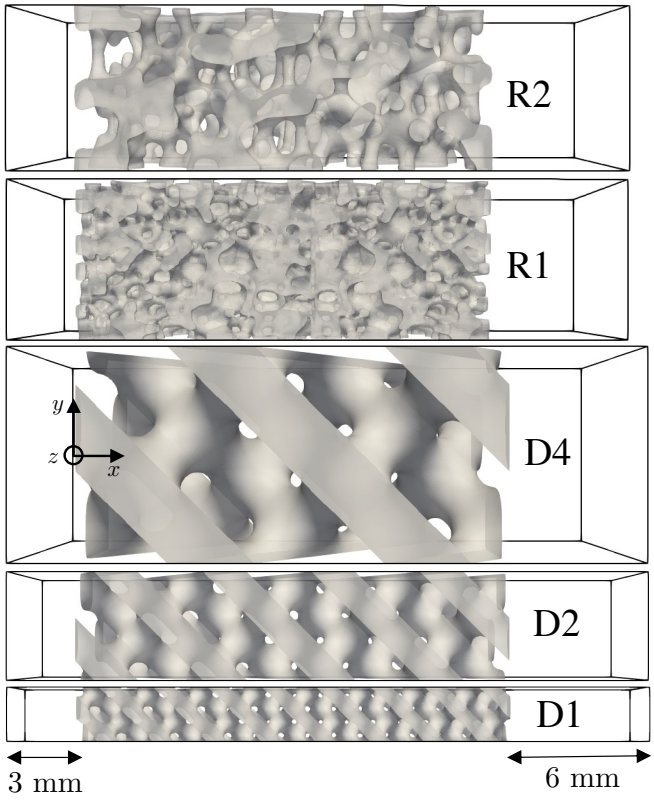

Figure 1: Computational domains. Flow from left to right.

With the idea of studying independently the influence of variations in pore size and topology upon volume-averaged modelling, five different computational domains are considered: R2, R1, D4, D2 and D1, as depicted in Fig. 1. Their general characteristics are given in Tab. 2. The mean porosity $\bar{\epsilon}$ represents the mean void fraction within the porous structure and L is the length of the solid matrix. The domains comprise gaseous inlet and outlet

Table 1: Literature review of DPLS for porous media combustion.

Ref.	**Study**	**Complex kinetics**	**Mesh (µm)**	**Domain (mm)**	**Radiation**
Sarhaoui and Kaviany [25]	2D DPLS and 1D VAM staggered arrangement of square rods	No	N.A.	5x1.5	No
Hackert et al. [12]	2D DPLS in tubes and discrete plates with/out heat losses	No	40	20x10	Yes
Yamamoto et al. [26]	3D DPLS regeneration process of diesel particulate filter	No	250	50x10x10	No
Bedoya et al. [16]	1D VAM, 3D DPLS and experiments for various burner geometries	No	160	divergent 65x(in: 1.1x9 – out: 28x9)	No
Jouybari et al. [27]	2D RANS staggered arrangement of square rods	No	N.A.	100x2.5	No
Dixon [28]	3D DPLS packed-bed steam reforming homog./heterog. react.	No	>1200	cyl. 650x150	No
Sirotkin et al. [14]	2D DPLS packed bed SPH filtr. combustion	No	160	40x20	No
Yakovlev et al. [18]	3D DPLS unsteady packed-bed combustion	Yes	< 500	35x35x100	Yes (gray)
Billerot et al. [17]	3D DPLS in lattice-based porous media	No	40	42.5x1.2x1.2	Yes (gray)
Liu et al. [15]	2D DPLS two-layered packed-bed combustion	No	> 200	5x140	Yes (gray)
Shi et al. [19]	1D VAM and 3D DPLS packed-bed reactor filtration combustion	No	~ 500	cyl. 353x38	Yes
Ferguson et al. [13]	2D DPLS packed bed Delaunay network for solid heat transport	Yes	< 100	40x20	No

regions of respectively 3 and 6 mm. The letter in their denomination refers

to their type of matrix topology. R geometries consist of Reticulated structures typical of porous burners - see for instance [16, 29] - acquired through X-Ray tomography (device: EasyTom XL, source: Hamamatsu MicroFocus, scanning parameters: 170 kV, 120 µA, 2200 images/turn, achieved resolution: 17 µm). D geometries consist of regular lattices obtained from the Diamond triply-periodic minimal surface:

$$\begin{aligned} \text{solid region} \iff & sin(kx)sin(ky)sin(kz) \\ & +sin(kx)cos(ky)cos(kz) \\ & +cos(kx)sin(ky)cos(kz) \\ & +cos(kx)cos(ky)sin(kz) > t, \end{aligned} \tag{1}$$

where k is the spatial wavenumber and here $t = 0.27$ yields a mean porosity $\bar{\epsilon}$ near 0.6. Similar regular geometries were studied experimentally in [30]. The associated numeral (1, 2 or 4) refers to their approximate mean pore diameter $\bar{d_p}$ in mm, computed by a local thickness filter on the final geometry. Fig. 2(a) shows the distribution of pore diameters and its mean value for the five cases and Fig. 2(b) plots the longitudinal evolution of volume-averaged porosity, showing slight variations that may favor flame anchoring at preferential locations.

The meshes consist of unstructured tetrahedra. In the gas phase, the prescribed mesh size is uniform (80 µm), yielding an error below 2% on flame speed at 300 K and 600 K in planar 1D adiabatic free flames. In the solid phase, the mesh size is similar (< 100 µm). This spatial resolution is much finer than most studies reported in Tab. 1. A mesh convergence study was performed down to 40 µm and it showed that the resolution of 80 µm is sufficient.

Due to heat recirculation, several convective time scales within the gas phase must be computed (*i.e.* several $\sim 10^{-2}$ s). The resulting computational cost for one simulation point is approximately 10^6 core-hours.

2.1.2. Gaseous phase

In the gaseous phase, the compressible reactive Navier-Stokes parallel solver AVBP is used with the TTGC scheme [31], which is third order in space and time. No subgrid scale model is used. Inlet and outlet boundaries are treated via the NSCBC formalism [32]. At the inlet, a CH_4-air mixture is injected at constant velocity U_{in} and temperature $T_{\text{in}} = 300$ K. At the outlet, a constant pressure $P_0 = 1$ atm is imposed. On the sides, symmetry

Table 2: Main mesh parameters for all cases.

	$\bar{d_p}$ (mm)	$\bar{\epsilon}$ (-)	L (mm)	nb. cells gas (million)	nb. cells solid (million)
R2	1.75	0.61	18.2	21.3	3.8
R1	1.08	0.59	18.1	19.9	7.0
D4	3.90	0.63	18.8	37.6	6.5
D2	2.02	0.62	18.8	4.8	2.5
D1	1.07	0.63	18.8	2.4	0.8

conditions are adopted. The pointwise (microscopic) governing equations in AVBP are:

$$\frac{\partial \rho_{g,k}}{\partial t} + \nabla \cdot (\rho_{g,k}\mathbf{u}) + \nabla \cdot \mathbf{J_k} - \dot{\omega}_k = 0, \tag{2}$$

$$\frac{\partial \rho_g \mathbf{u}}{\partial t} + \nabla \cdot (\rho_g \mathbf{u}\mathbf{u}) + \nabla \cdot \left[P\underline{\underline{\mathbf{I}}} - \underline{\underline{\boldsymbol{\tau}}}\right] = 0, \tag{3}$$

$$\frac{\partial \rho_g E}{\partial t} + \nabla \cdot (\rho_g E \mathbf{u}) + \nabla \cdot \left[\mathbf{u} \cdot \left(P\underline{\underline{\mathbf{I}}} - \underline{\underline{\boldsymbol{\tau}}}\right) + \mathbf{q}\right] - \dot{\omega}_T^0 = 0. \tag{4}$$

where:

- the fluid is Newtonian ;
- volume forces such as gravitation and radiation in the gas phase are neglected ;
- E is the total non-chemical energy per mass unit, ρ_g the gas density, $\mathbf{u}$ the velocity field, $\underline{\underline{\boldsymbol{\tau}}}$ the viscous stress tensor ;
- the fluid is a mixture of perfect gases ;
- diffusion is computed by using the Hirschfelder and Curtis approximation:

$$\mathbf{J_k} = -\rho_g \left(D_k \frac{W_k}{W} \nabla X_k - Y_k \mathbf{V^c} \right), \tag{5}$$

  where the correction velocity $\mathbf{V^c}$ ensures mass conservation:

$$\mathbf{V^c} = \sum_{k=1}^{N} D_k \frac{W_k}{W} \nabla X_k. \tag{6}$$

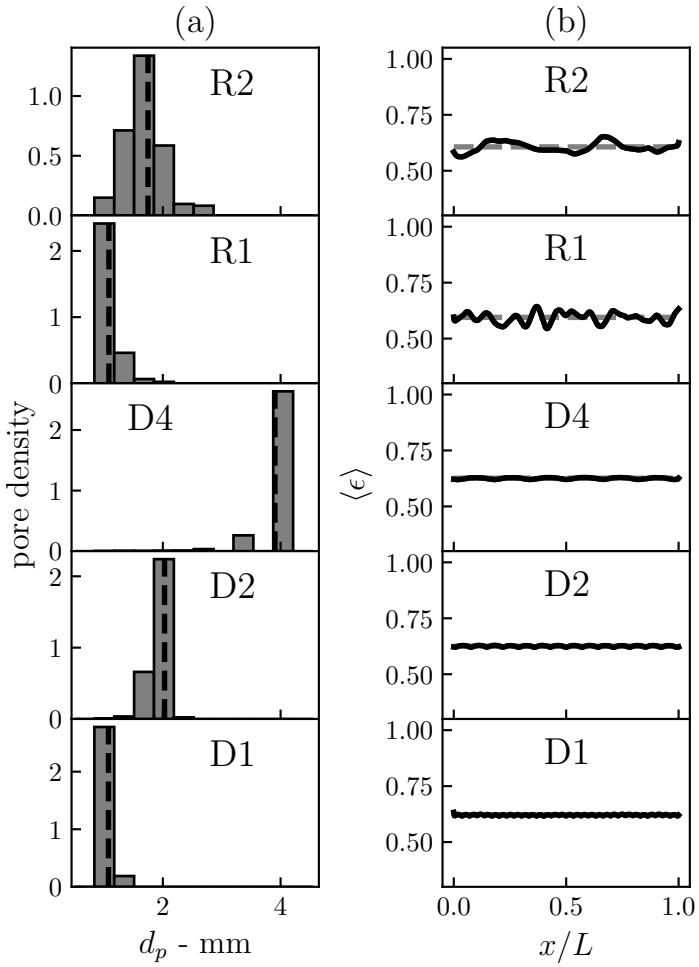

Figure 2: Local characterization of the geometries. (a) pore density versus local pore diameter d_p and (b) longitudinal evolution of volume-averaged averaged porosity $\langle\epsilon\rangle$ (average defined at REV scale, defined in Sec. 2.2).

- the heat flux $\mathbf{q}$ is composed of the Fourier heat flux with a conductivity λ_g, plus the flux related to preferential diffusion of the sensible species enthalpies $h_{s,k}$:

$$\mathbf{q} = -\lambda_g \nabla T_g + \sum_k \mathbf{J_k} h_{s,k}. \tag{7}$$

- transport is simplified assuming constant Prandtl (Pr = 0.7) and species

Schmidt numbers (Sc_k):

$$\mathrm{Sc}_k = \mathrm{Pr} \cdot \mathrm{Le}_k, \tag{8}$$

so that the Lewis number Le_k of individual species is also constant.

- the heat release per unit volume $\dot{\omega}_T^0$ is given by the formation enthalpies (cf. Eq. (1.68) in [33]):

$$\dot{\omega}_T^0 = -\sum_k \Delta h_k^{f,0}\, \dot{\omega}_k. \tag{9}$$

- viscosity is computed using a power law:

$$\mu = \mu_{\mathrm{ref}} \left(\frac{T_g}{T_{\mathrm{ref},\mu}} \right)^{n_\mu}. \tag{10}$$

For the present mixture, adapted values are $\mu_{\mathrm{ref}} = 7.05 \times 10^{-5}\,\mathrm{kg\,m^{-1}\,s^{-1}}$, $T_{\mathrm{ref},\mu} = 2205$ K and $n_\mu = 0.64$.

In order to simulate a realistic behavior of the flame front, an Analytically-Reduced Chemistry (ARC) is derived from a hierarchical kinetic mechanism developed by the CRECK modelling Group [34]. The reduction is performed using ARCANE [35], based on DRGEP method [36] and the Quasi-Steady-State formalism (QSS) [37]. The reduced scheme, labelled CH4_15_138_9_AP, comprises 15 transported species and 9 QSS species for a total of 138 reversible reactions. The kinetic database, along with additional information on reduction targets and validations are available in Apps. A and B of the Supplementary Material.

The main characteristics of the mixture used in this study, namely inlet temperature T_{in}, equivalence ratio ϕ, flame speed S_L^0, thermal thickness δ_L^0 and adiabatic temperature T_{ad} are given in Tab. 3.

Table 3: Mixture properties at ambient pressure $P_0 = 1\,\mathrm{atm}$.

T_{in}	ϕ	S_L^0	δ_L^0	T_{ad}
300 K	0.72	20 $\mathrm{cm\,s^{-1}}$	0.63 mm	1883 K

Because the response of the flame to preheating is central in PMC, Fig. 3 presents the flame acceleration in terms of mass flux, $\Gamma_p = \dot{m}/\rho_{\mathrm{in}} S_L^0$, for the considered mixture. It is observed that the ARC mechanism adequately retrieves the response to the temperature, noted $T_{\mathrm{preheating}}$ in Fig. 3 for later use. An exponent-based best fit of Γ_p is shown and used for post-processing.

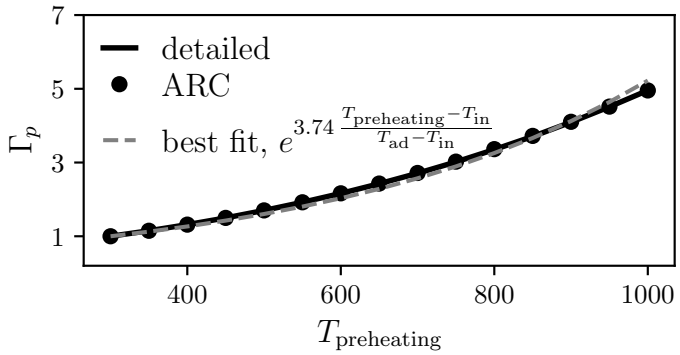

Figure 3: Flame acceleration due to preheating.

2.1.3. Solid phase

In the solid phase, the solver AVTP [38] is used to compute the heat equation assuming Fourier's law:

$$\rho_s c_{p_s} \frac{\partial T_s}{\partial t} - \nabla \cdot [\lambda_s \nabla T_s] = 0. \tag{11}$$

Spatial discretization uses second-order Galerkin diffusion scheme, and time integration is performed with an implicit first-order forward Euler scheme. The inversion of the system is achieved through a parallel matrix-free conjugate-gradient method [39]. Adiabatic walls are prescribed on the sides. The solid conductivity λ_s is constant and set to $10\,\mathrm{W\,m^{-1}\,K}$.

2.1.4. Radiation

Three contributions of internal radiative heat transfer may be considered in PMC. The first two are gas/gas and gas/solid heat transfer, which can be neglected under the assumption that the gases are transparent. This approximation is done in virtually all studies and is deemed accurate for lean methane combustion. Regarding solid/solid heat transfer, it is usually assumed that the porous network acts as an effective medium where the Radiative Transfer Equation (RTE) applies with effective macroscale coefficients. The determination of these effective properties, and the conditions under which this modelling is valid is an area of active research. Nevertheless, it has become standard practice to solve the RTE or one of its approximations in VAM, which allows to retrieve with more or less accuracy experimental temperature profiles [40–42]. The influence of radiation on the stability of

burners of finite length was studied by Sathe et al. [23] and it was found that the qualitative behavior of the flame is lowly affected by radiation. Similar conclusions were obtained by Mendes et al. [43]. While radiation does affect the macroscopic temperature profile via external heat losses and increased heat recirculation, it is not expected to directly affect the structure of the flame front at the pore scale. In this work, radiation is not considered because the focus is on the structure of the flame front and its consequences on the derivation of VAM. The absolute level of heat recirculation might be different to that in a hypothetical corresponding experiment but the comparison between pore-resolved and VAM simulation is consistent. Moreover, any modelling issue in the VAM found without radiation is unlikely to be tamed by its inclusion in the model.

2.1.5. Coupling strategy

The two softwares AVBP and AVTP are coupled through the CWIPI library [38]. At the gas/solid boundary $\mathcal{A}_{gs}$, AVTP imposes the temperature and AVBP the energy flux, so that:

$$\lambda_g \nabla T_g \cdot \mathbf{n_{gs}} = \lambda_s \nabla T_s \cdot \mathbf{n_{gs}} \qquad \text{and} \qquad T_s = T_g \qquad \text{on } \mathcal{A}_{gs}, \tag{12}$$

where $\mathbf{n_{gs}}$ is the unit normal vector gas $\rightarrow$ solid, as shown in Fig. 4. The AVBP-AVTP coupling strategy was tested on various configurations and shows good agreement with experimental data [44]. Since only steady states are of interest, the two solvers are not synchronized and the solid is typically computed over a time span several thousands of times larger than the fluid. This time-decoupling strategy was used in packed-bed combustion [18] and yielded the same results than matched time steps. In addition, the no-slip and non-permeable-inert conditions at the gas/solid interface imposes:

$$\mathbf{u} = 0 \qquad \text{and} \qquad \mathbf{J_k} \cdot \mathbf{n_{gs}} = 0 \qquad \text{on } \mathcal{A}_{gs}. \tag{13}$$

2.2. 1D Volume-Averaged Model

Fig. 4 presents the principle of volume-averaging used in the present work, adapted to the framework of porous burners with a preferential flow direction (here x). The integration domain, centered on $\mathbf{x}$, is also called Representative Elementary Volume (REV), and has a thickness of $2\,r_0$. In our simulations it was found that a value of $r_0 \sim \bar{d}_p/2$ would smooth local variations and avoid macroscopic gradients so the typical size of the REV is chosen to be equal to $\bar{d}_p$ for all domains. Moderate modifications to this integration size led to

neither qualitatively nor quantitatively different conclusions. The integration is performed over $\mathbf{y}$. The intrinsic averages in the gas $\langle\cdot\rangle^g$ and solid $\langle\cdot\rangle^s$ phases are defined by:

$$\langle\psi\rangle^g = \frac{1}{\mathcal{V}_g}\int_{\mathcal{V}_g}\psi\,\mathrm{d}V \qquad \text{and} \qquad \langle\psi\rangle^s = \frac{1}{\mathcal{V}_s}\int_{\mathcal{V}_s}\psi\,\mathrm{d}V, \tag{14}$$

where $\mathcal{V}_g$ and $\mathcal{V}_s$ are the gas and solid regions contained within the REV.

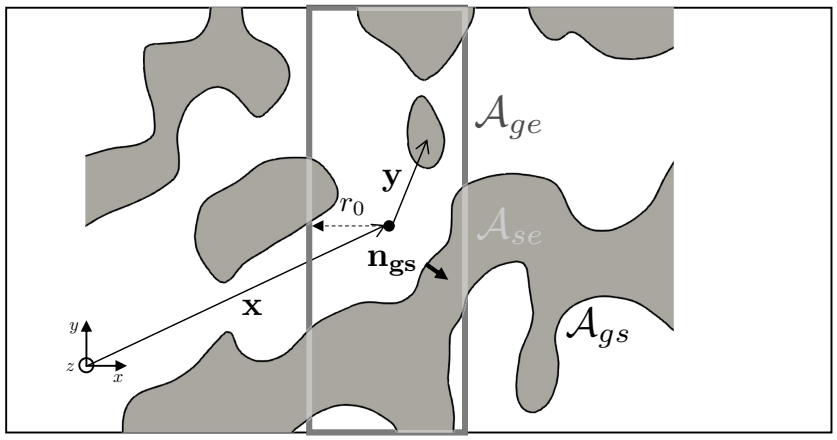

Figure 4: Principle of volume-averaging and shape of the REV.

2.2.1. Governing equations

The classical 1D volume-averaged equations for porous media combustion are [4, 16, 29, 41, 42, 45]:

$$\epsilon\,\langle\rho_g\rangle^g\,\langle u\rangle^g\,\partial_x\,\langle Y_k\rangle^g + \partial_x\left[\epsilon J_k^{\mathrm{eff}}\right] - \epsilon\,\langle\dot{\omega}_k\rangle^g = 0, \tag{15}$$

$$\begin{aligned}\epsilon\,\langle\rho_g\rangle^g\,\langle u\rangle^g\,\left\langle c_{p_g}\right\rangle^g\,\partial_x\,\langle T_g\rangle^g - \partial_x\left[\epsilon\,\langle\rho_g\rangle^g\left\langle c_{p_g}\right\rangle^g D_{th}^{\mathrm{eff}}\partial_x\,\langle T_g\rangle^g\right]\\ + \sum\nolimits_k \epsilon\left\langle c_{p_g,k}\right\rangle^g J_k^{\mathrm{eff}}\partial_x\,\langle T_g\rangle^g + \epsilon\,\langle\dot{\omega}_T\rangle^g + h_V(\langle T_g\rangle^g - \langle T_s\rangle^s) = 0,\end{aligned} \tag{16}$$

$$\partial_x\left[\lambda_s^{\mathrm{eff}}\partial_x\,\langle T_s\rangle^s\right] + h_V(\langle T_g\rangle^g - \langle T_s\rangle^s) = 0, \tag{17}$$

where ϵ is the local porosity, $\langle T_s\rangle^s$ the solid temperature, h_V the interphase heat transfer coefficient. The macroscale effective diffusive flux J_k^{eff} is:

$$J_k^{\mathrm{eff}} = -\,\langle\rho_g\rangle^g\left[D_k^{\mathrm{eff}}\frac{W_k}{\langle W\rangle^g}\partial_x\,\langle X_k\rangle^g - \langle Y_k\rangle^g\,V_c^{\mathrm{eff}}\right], \tag{18}$$

where $\langle W \rangle^g$ is the mean molar mass, $\langle X_k \rangle^g$ the molar fractions and V_c^{eff} the macroscale correction velocity:

$$V_c^{\text{eff}} = \sum_{k=1}^{N} D_k^{\text{eff}} \frac{W_k}{\langle W \rangle^g} \partial_x \langle X_k \rangle^g . \tag{19}$$

The dispersion coefficient D^{dis}, defined later in Section 3.1.2, gives:

$$D_k^{\text{eff}} = \langle D_k \rangle^g + D^{\text{dis}} \tag{20}$$

and:

$$D_{th}^{\text{eff}} = \frac{\langle \lambda_g \rangle^g}{\langle \rho_g \rangle^g \left\langle c_{p_g} \right\rangle^g} + D^{\text{dis}}. \tag{21}$$

These equations are standard but not derived via an exact mathematical procedure since commutations between averages, products and operators were required. The resulting macroscopic models therefore include some level of approximation, which has been extensively discussed in the scientific community and the dispersion coefficient D^{dis} is an important model parameter. From the perspective of combustion, the main requirement is to model $\langle \dot{\omega}_k \rangle^g$ and a simple commutation of the averaging operator is usually assumed, which yields:

$$\langle \dot{\omega}_k \rangle^g = \dot{\omega}_k \left(\langle \rho_g \rangle^g , \langle T_g \rangle^g , \langle Y_k \rangle^g \right) . \tag{22}$$

The corresponding volume-averaged heat release rate is:

$$\langle \dot{\omega}_T \rangle^g = \sum\nolimits_k \langle h_k \rangle^g \langle \dot{\omega}_k \rangle^g . \tag{23}$$

Unlike Eq. (4), Eq. (16) is based on the temperature, therefore the volume-averaged heat release rate is in fact rigorously equal to:

$$\begin{aligned} \langle \dot{\omega}_T \rangle^g &= \sum\nolimits_k \langle h_{s,k} \rangle^g \langle \dot{\omega}_k \rangle^g + \left\langle \dot{\omega}_T^0 \right\rangle^g \\ &= \sum\nolimits_k \langle h_{s,k} \rangle^g \langle \dot{\omega}_k \rangle^g + \sum\nolimits_k \Delta h_k^{f,0}(T_{\text{ref},h}) \langle \dot{\omega}_k \rangle^g , \end{aligned} \tag{24}$$

but for simplicity and because the influence of sensible enthalpies is largely negligible, it is assumed that $\langle \dot{\omega}_T \rangle^g = \langle \dot{\omega}_T^0 \rangle^g$. For the numerical resolution, the software Cantera [46] is adapted to resolve the kinetic scheme of Sec. 2.1.2 and the VAM governing equations. Standard numerical integration from Cantera is used, including pseudo-time stepping approach

and adaptative refinement. The initial mesh size is uniform (60 µm, *i.e.* approximately 500 grid points, with extra points added near the boundaries to help convergence). The initial solutions are set by constructing solid and gaseous superadiabatic profiles from the theoretical framework and formulae derived by the authors in [22]. For numerical stability, the field of porosity ϵ is smoothed over 0.1 mm in CANTERA at the inlet/outlet boundaries of the solid. Also, porosity is assumed constant at the core of the solid $\epsilon = \bar{\epsilon}$. Comparing the 3D pore-scale solution obtained with AVBP, CANTERA assumes a constant pressure and neglects viscous heating, two assumptions which introduce negligible errors in the present configurations.

3. Effective properties and DPLS results

3.1. Macroscopic effective properties

There are several methodologies to determine the effective properties to be used in VAM. The first one is to make use of existing correlations, determined experimentally or numerically. For example, there are many correlations for the heat transfer coefficient h_V [47–50], each having its own range of validity in terms of temperature, flow rate, porosity, pore size, etc. Another example, in asymptotic analyses it is often assumed that the effective conductivity depends on the porosity via $\lambda_s^{\text{eff}} = (1-\epsilon)\lambda_s$ [22, 51], an estimation retrieved during the upscaling procedure by neglecting local deviations. Correlations for dispersion are also available [52]. Such estimations are typically quite accurate in terms of order of magnitude.

A second methodology, adopted in this work, is to compute the effective parameters of the specific cases by performing *independent* numerical simulations in the solid and gas phases [29]. Although it is not ensured that the magnitude and functional forms of the effective macroscale models are rigorously the same in non-reactive (independent) and reactive (coupled) simulations, this corresponds to the classical methodology used to date in porous media combustion. The values obtained are reported in Tab. 4 and the procedure to obtain them is now described.

3.1.1. Effective thermal conductivity

The solid effective conductivity λ_s^{eff} is determined with transient simulations in the solid domain via the excitation of the first longitudinal cosine mode with adiabatic boundary conditions. The benefit of this method is the

Table 4: Macroscale properties of the various domains.

	h_V $(\mathrm{W\,m^{-3}\,K^{-1}})$	λ_s^{eff} $(\mathrm{W\,m^{-1}\,K^{-1}})$	A^{dis} $(\mathrm{m^2\,s^{-1}})$
R2	10×10^4	2.3	26.1×10^{-4}
R1	41×10^4	2.7	14.3×10^{-4}
D4	6×10^4	1.8	7.3×10^{-4}
D2	23×10^4	1.7	6.2×10^{-4}
D1	36×10^4	2.0	3.4×10^{-4}

simplicity of the temporal evolution of the system. Indeed, by setting the initial temperature at time $t = 0$ as:

$$T_s(x) = T_s^0 + \Delta T_s \cos\left(\frac{\pi x}{L}\right), \tag{25}$$

the analytical solution of the equivalent, macroscopic heat equation is:

$$\langle T_s \rangle^s (x) = T_s^0 + \Delta T_s \cos\left(\frac{\pi x}{L}\right) \exp\left(\frac{-\pi^2 \lambda_s^{\mathrm{eff}} t}{(1-\bar{\epsilon})\rho_s c_{p_s} L^2}\right), \tag{26}$$

which allows to fit λ_s^{eff}. In the simulations the values $T_s^0 = 600\,\mathrm{K}$ and $\Delta T_s = 100\,\mathrm{K}$ are used, but because of the linearity of the heat equation they do not impact the solution. A comparison between the evolution of $\langle T_s \rangle^s$ in the simulations and a best fit of λ_s^{eff} based on Eq. (26) is shown in Fig. 5 for domain R1. Similar agreement is found for all the cases.

3.1.2. Dispersion coefficient

The numerical procedure for the determination of the hydrodynamic dispersion is illustrated in Fig. 6. From a steady-state non-reacting solution ($T_g^0 = 300$ K), a small discontinuity of temperature ($\delta T_g = 10$ K) is imposed at time $t = 0$, with adiabatic conditions at the fluid-solid boundary. The broadening of the volume-averaged temperature profile depends on the hydrodynamic dispersion. Following [16], the dispersion coefficient D^{dis} may be written as:

$$D^{\mathrm{dis}} = 0.5 \cdot A^{\mathrm{dis}} \cdot \langle u \rangle^g . \tag{27}$$

In the macroscale equation, the resulting thermal effective diffusion coefficient is therefore assumed to be of the form:

$$D_{th}^{\mathrm{eff}} = \frac{\langle \lambda_g \rangle^g}{\langle \rho_g \rangle^g \left\langle c_{p_g} \right\rangle^g} + 0.5 \cdot A^{\mathrm{dis}} \cdot \langle u \rangle^g , \tag{28}$$

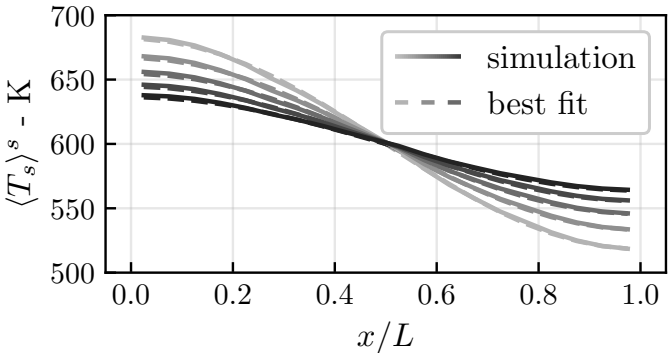

Figure 5: Volume-averaged solid temperature profile: fit of effective thermal conductivity for domain R1 (time computed 21 s). Profiles evenly distributed in time.

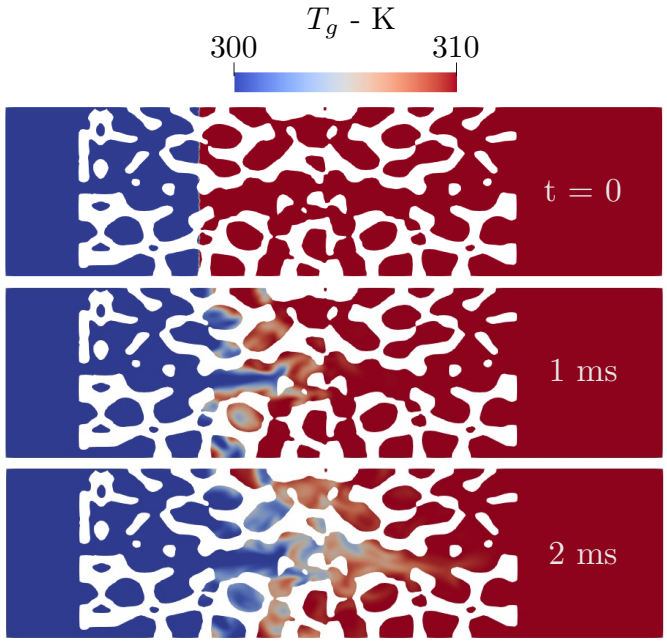

Figure 6: Illustration of dispersion in physical space: longitudinal cuts of temperature. Domain R1, from $t = 0$ to 2 ms, inlet velocity $U_{\text{in}} = 1\,\text{m}\,\text{s}^{-1}$.

where the volume-averaged values vary only slightly due to the temperature variations. In the limit $\langle u \rangle^g \to 0$, the intrinsic diffusivity of gas phase is retrieved, which boils down to neglecting the effects of tortuosity at ultra-low velocities [52]. At the macroscopic scale, the transient governing equation

of convection-diffusion is:

$$\frac{\partial \langle T_g \rangle^g}{\partial t} - D_{th}^{\text{eff}} \frac{\partial^2 \langle T_g \rangle^g}{\partial x'^2} = 0, \tag{29}$$

where $x' = x + \langle u \rangle^g t$ is the referential of the moving initial pulse. Its solution can be found via a Fourier transform, supposing an infinite medium, which in physical space reads:

$$\langle T_g \rangle^g (x', t) = T_g^0 + \frac{\delta T_g}{2} \sqrt{\frac{1}{\pi D_{th}^{\text{eff}} t}} \int_{-\infty}^{0} \exp\left[-\frac{(x' - y')^2}{4 D_{th}^{\text{eff}} t} \right] \mathrm{d}y', \tag{30}$$

where y' is a dummy integration variable. In the reference frame, this leads to:

$$\langle T_g \rangle^g (x, t) = T_0 + \frac{\delta T_g}{2} \left[1 - \operatorname{erf}\left(\frac{x - \langle u \rangle^g t}{2\sqrt{D^{\text{eff}} t}} \right) \right]. \tag{31}$$

A best fit of Eq. (31), together with Eq. (28) onto the simulation is shown in Fig. 7 for domain R1, where the three solutions fields of Fig. 6 correspond to the three leftmost profiles.

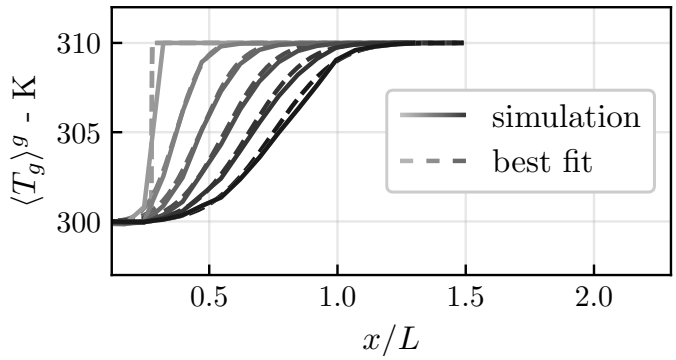

Figure 7: Volume-averaged gas temperature versus reduced abscissa: fit of dispersion coefficient for domain R1 ($U_{\text{in}} = 1\,\text{m}\,\text{s}^{-1}$, time computed 5 ms). Profiles evenly distributed in time: the first three profiles on the left correspond to that of Fig. 6.

3.1.3. Interphase heat transfer coefficient

The macroscale heat transfer per unit volume from the gas to the solid Q_{gs} is often modelled through a heat transfer coefficient h_V as:

$$Q_{gs} = h_V \left[\langle T_g \rangle^g - \langle T_s \rangle^s \right]. \tag{32}$$

In this work, unlike λ_s^{eff} and A^{dis}, the interphase volume heat transfer coefficient h_V is fitted directly on the reacting DPLS, and not determined independently. This is due to the large discrepancies observed between attempted gas-only simulations (*e.g.* relaxation of gas temperature into a hot solid) and reactive gas-solid simulations. A best fit of Eq. (32) is shown in Fig. 8 for domain D2. The agreement is not as good in the combustion zone ($x/L \sim 0.6$) but for the important preheating region the correlation is deemed sufficient. Other correlations have been tested, including dependencies upon the Reynolds number and thermal conductivity, with minor improvements.

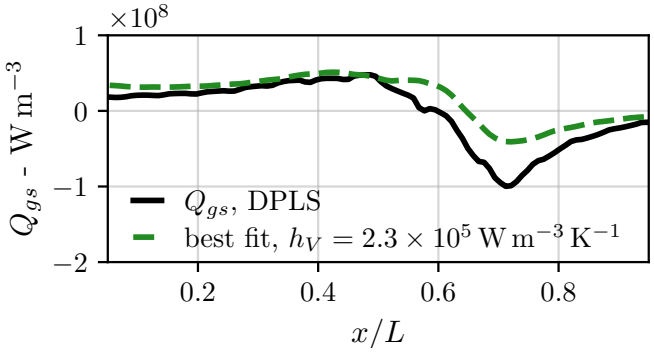

Figure 8: Longitudinal evolution of interphase heat exchange per unit volume and fit with constant h_V on domain D2.

3.2. Structure of the submerged flame

The structure of flames embedded in the solid matrix is now investigated. For each case, a steady-state condition for which the flame is fully submerged is presented. The corresponding values for inlet velocities U_{in} and pore-based Reynolds numbers $\text{Re}_p = \rho_{\text{in}} U_{\text{in}} \bar{d}_p / \mu_{\text{in}}$ are given in Tab. 5. Steadiness is assessed through both macroscopic values such as total kinetic energy, total heat release and total interphase heat transfer, as well as local probes in the flow to detect local fluctuations. Notably, since the solid is globally adiabatic, a good indicator of convergence is found to be the integral of the interphase heat transfer Q_{gs}, which is imposed to be below 1% of the total chemical energy release per time unit. For domain D4, the Reynolds number has been artificially reduced to tame a slight unsteadiness which was originally observed. This is achieved by an increase in the dynamic

viscosity μ by a factor of 3. The other intrinsic gas properties, such as thermal and species diffusivities, were kept constant by increasing the Prandtl and Schmidt numbers of the same factor. It was checked in a 1D simulation that the resulting reference flame speed was unaffected. Despite this small change in operating condition, case D4 is relevant to study the influence of the ratio of pore size to flame thickness whilst remaining within steady-state framework. One should keep in mind, however, that steady-state volume-averaged models may not be valid for burners of overly large pores sizes (here D4 corresponds approximately to 10-15 PPI), a point which is rarely discussed in the literature.

Table 5: Inlet velocities U_{in} and pore-based Reynolds numbers Re_p.

	R2	R1	D4	D2	D1
U_{in} - $\text{m}\,\text{s}^{-1}$	0.60	0.65	0.80	0.60	0.65
Re_p	56.1	37.5	55.5	64.7	37.1

A 3D view of the solutions is shown in Fig. 9, where the reaction zone is identified via a heat-release-rate isosurface colored in black. Both streamlines and the solid are colored by temperature. It is observed that the flame fronts are quite convoluted and spatially distributed along the longitudinal axis. The level of preheating of the gaseous phase can not be appreciated on these 3D plots but a quantitative analysis shows that it reduces the thermal thickness of the flame front below the reference value $\delta_L^0 = 0.63\,\text{mm}$, typically near 0.4-0.5 mm. From the streamlines it is inferred that the flow is more tortuous in R than D domains, which is coherent with their value of A^{dis}.

The anchoring of the flame fronts is further investigated in Fig. 10, which shows longitudinal cuts of gas and solid temperatures (blue to red) with the field of heat release rate as a black overlay. The material boundaries are colored by the magnitude of the heat flux from the gas to the solid (green to purple). Positive heat fluxes are larger near the flame base while negative values are typically encountered at locations facing the inflow. Superadiabatic temperatures are observed in the vicinity of the flame front but the return to equilibrium typically occurs within a pore or two. Finally, in domain D4 the flame front is so distorted that it can extend over a whole pore, showing finger-like structures reminiscent of the works of [21] in a thin-layered porous burner.

4. Comparison of DPLS and VAM results

In Sec. 3.2, potential discrepancies between the classical derivation hypotheses of the VAM and the observed flame structure in the DPLS have been pointed out, such as the presence of sharp, wrinkled, and longitudinally-distributed flame fronts, but also local flame/wall interactions. The quantitative evaluation of these effects is now addressed: the predictions of the VAM using Eq. (22) in terms of burning rate and axial profiles are discussed and compared to the DPLS.

4.1. Burning rate

The burning rate of flames within porous media is known to be substantially larger than the corresponding 1D adiabatic free-flame and the resulting acceleration may be measured by a parameter Γ defined as a ratio of velocities or mass flow rates:

$$\Gamma = \frac{U_{\text{in}}}{\bar{\epsilon}\, S_L^0} = \frac{\dot{M}_{\text{in}}}{\bar{\epsilon}\, \dot{m}_0 \mathcal{A}_T}. \tag{33}$$

U_{in} and $\dot{M}_{\text{in}}$ are the inlet velocity and mass flow rate, $\mathcal{A}_T$ the cross-section area, S_L^0 and $\dot{m}_0 = \rho_{\text{in}} S_L^0$ the corresponding 1D adiabatic free flame speed and mass flux per surface unit. Note that, much like for RANS and LES frameworks in turbulent combustion, the averaging or filtering procedure is problematic for the reaction terms. The reaction rates are strongly non-linear and Γ is directly related to their integral.

Fig. 11 compares values of Γ in the DPLS to the corresponding VAM simulations, obtained by imposing the same axial location of maximum heat release rate. Another strategy would be to compare flame positions for the same value of Γ, but it does not always lead to stable solutions with an embedded flame in the VAM. The acceleration measured in the DPLS goes from 4.76 for case D2 to 6.35 for D4. These values are typical of experimental observations though, for the lack of radiation in the present simulations, there is no claim of quantitative accuracy. The largest Γ value for case D4 can be attributed to the larger surface convolution visible in Fig. 10. In both R and D topologies, reducing the pore size from 2 to 1 mm increases Γ. This may be attributed to increasing interphase heat exchange for decreasing pore size, but given the simultaneous variations in flame position between the cases (see Fig. 9) and increasing wall quenching, general trends concerning the influence of pore size on Γ cannot be drawn.

Overall, the differences in Γ values between DPLS and VAM are inconsistent among the cases and can be as large as 20% in either over- or under-prediction. Over-predictions are only observed in R geometries, and this can be attributed to their higher dispersion coefficient (see Tab. 4) which increases thermal diffusivity in the VAM hence consumption speeds. However, there is no evidence in the DPLS that Γ is governed by macroscale dispersion: between R and D cases, for same pore size and same flame position (see Fig. 9), Γ values are nearly equal. Because the corresponding VAM fed with different intensities of dispersion show different Γ values, this suggests that dispersion does not drive macroscale burning rate, which is consistent with the idea of localized thin flame fronts.

4.2. Longitudinal profiles

The comparison between DPLS and VAM using Eq. (22) is now performed on the longitudinal evolution of relevant variables. First, the solid and gas temperature profiles are presented in Fig. 12 for case D2. Despite the good agreement on the prediction of Γ in this case (see Fig. 11), the axial evolution of the temperature is quite different in the DPLS and VAM: this suggests that the simultaneous prediction of the physical profiles and of the global burning rate is difficult, and that the agreement on Γ partly originates from error cancellation. The agreement is best for the solid, with comparable gradients despite a significant underestimation in the VAM. Regarding the gas phase, the VAM profile is much steeper, which is attributed to the longitudinal distribution of the flame fronts observed in Figs. 9 and 10. It is also pointed out that on these averaged profiles, the local superadiabatic pockets observed in the DPLS are smoothed out. The other cases are not presented but show similar trends.

The longitudinal evolution of the heat release rate is presented in Fig. 13. As anticipated after the analysis of the gas temperature profiles, DPLS and VAM predictions are very different. In the VAM the HRR is steep and localized while it is three to four times wider in the DPLS. Nevertheless, their integrals are very close since the two models have nearly identical values of Γ. Again, it is a difference related to the absence of flame front distribution in the VAM.

This modelling difficulty can be further illustrated by *a priori* analysis on the reaction rates. Fig. 14 compares the profiles of DPLS volume-averaged heat release rate $\langle \dot{\omega}_T \rangle^g$ and heat release rate computed using the volume-averaged density, temperature and species mass fractions $\dot{\omega}_T(\langle \cdot \rangle^g)$. It is ob-

served that the *a priori* value $\dot{\omega}_T(\langle\cdot\rangle^g)$ systematically precedes and exceeds $\langle\dot{\omega}_T\rangle^g$. This can be attributed to flame wrinkling, but the also to the axial distribution of the combustion fronts: the upstream flame pockets intensify the exponential of temperature in the Arrhenius terms. It implies that the classical commutation assumption between reaction rates and their volume-average of Eq. (22), *i.e.* the absence of combustion model, is incorrect.

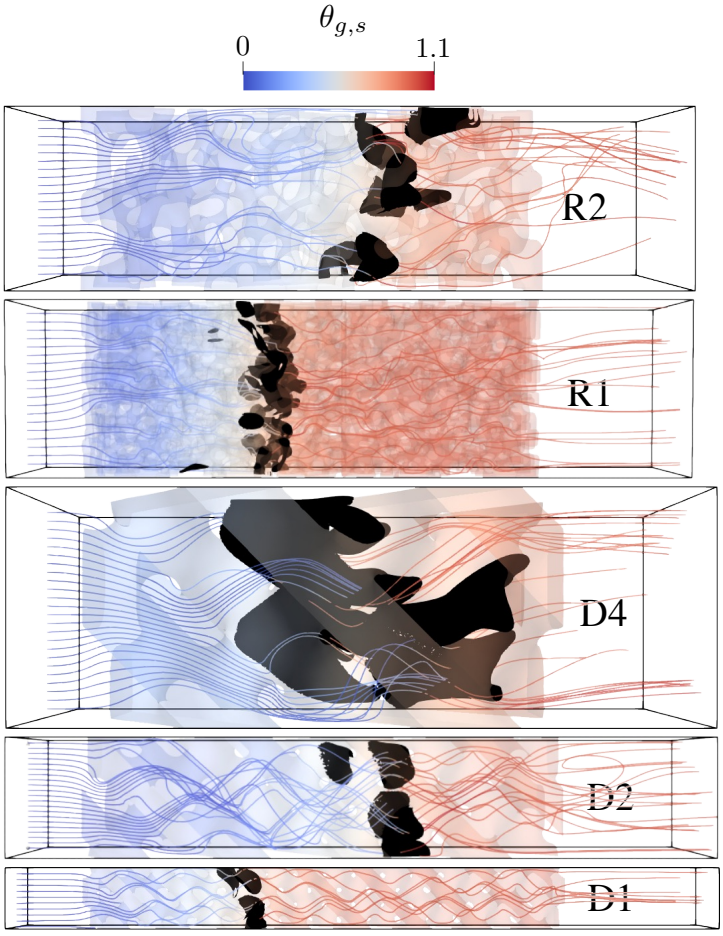

Figure 9: 3D view of the steady-state solutions for all cases. Streamlines and solid colored by temperature. Black iso-surface of heat release rate at $3 \times 10^9\,\mathrm{W\,m^{-3}}$.

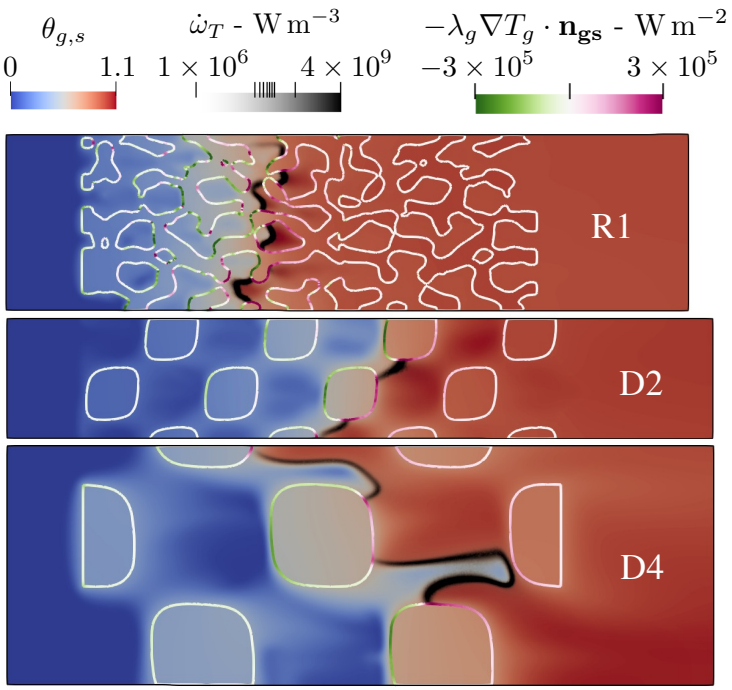

Figure 10: Longitudinal cuts of gas and solid temperature fields, heat release rate and interphase heat transfer at the walls.

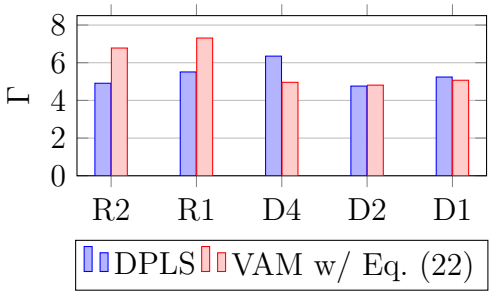

Figure 11: DPLS *vs.* VAM with properties of Tab. 4.

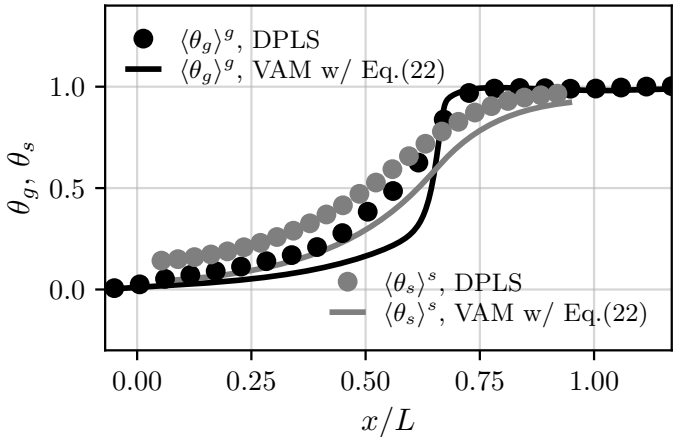

Figure 12: Gas/solid temperature profiles, DPLS *vs.* VAM, domain D2.

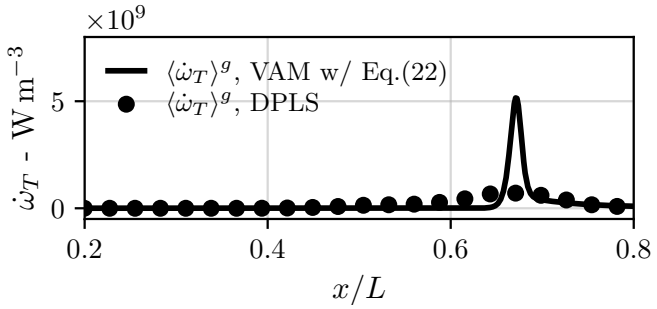

Figure 13: Average HRR in the DPLS *vs.* HRR computed in the VAM, domain D2.

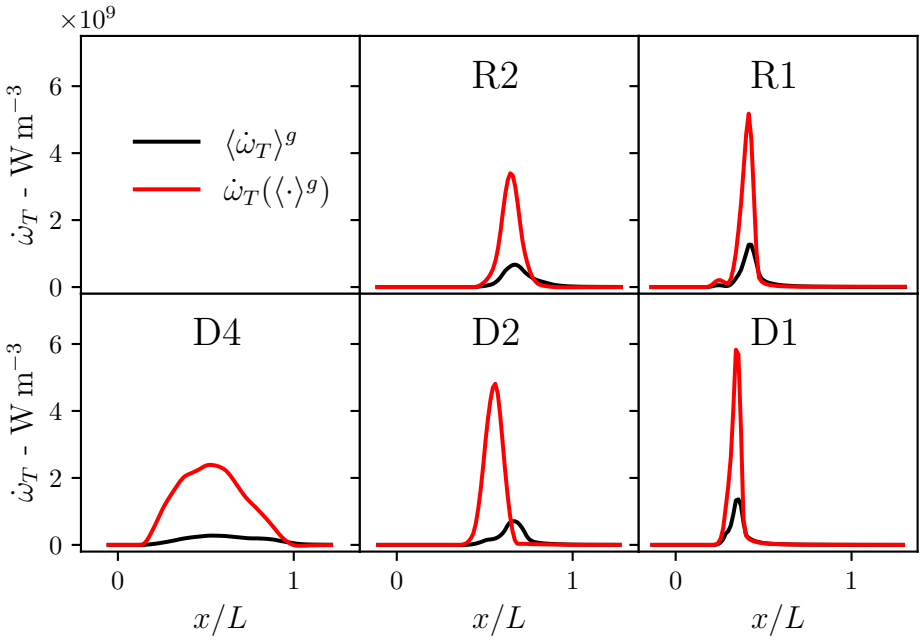

Figure 14: Evaluation of the commutation error for heat release rate (*a priori* analysis).

5. A flamelet-based strategy for the VAM

Including quantitatively the influence of non-planar and axially-distributed flame fronts in the VAM seems difficult. One may be tempted to increase the gas diffusion in order to widen the temperature profile, but this would affect Γ, and is not easy to justify from known macroscopic parameters. On the other hand, it has been pointed out that dispersion has potentially a wrong phenomenology and magnitude in the VAM, associated to the fact that volume-averaged models for PMC are aggregates of several macroscopic terms whose interactions are important. These issues in mind, and starting from the idea that combustion does not occur in volume at REV scale in the present cases, the following sections proposes to study PMC under the framework of flamelets. This leads to an expression for $\langle \dot{\omega}_k \rangle^g$ aimed at reproducing the phenomenology and quantitative value for burning rate Γ in the VAM. It is based on the assumptions that the flame fronts are thin and that preheating is the leading-order phenomena both in the VAM and DPLS. It accounts for the influence of flame wrinkling and removes the unwanted acceleration related to hydrodynamic dispersion.

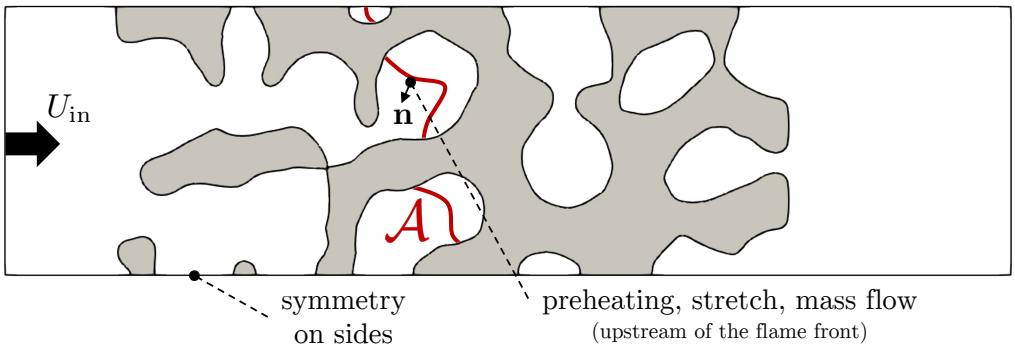

Figure 15: Principle of flamelet analysis in the DPLS.

5.1. Flamelet approach: theory

The question to investigate is: if the flame does not burn in volume at REV scale, then what are the factors that account for its global burning rate Γ? As suggested by the DPLS results, this is now done in the framework of *flamelets*. The concept is illustrated in Fig. 15, where the thin flame surface is noted $\mathcal{A}$ and represented in red. On $\mathcal{A}$, the normal to the flame

front pointing towards the fresh gases is noted $\mathbf{n}$ and the mass flow rate per surface unit $\dot{m}_n$ is:

$$\dot{m}_n = -\rho_g \, \mathbf{u} \cdot \mathbf{n}. \tag{34}$$

Just upstream of the flame front, important quantities such as the (preheated) temperature $T_{\text{preheating}}$ and stretch κ may be measured. Under the assumption that the flame fronts are locally adiabatic and by neglecting the effects of stretch for now, a simple model is proposed:

$$\dot{m}_n = \dot{m}_0 \cdot \Gamma_p(T_{\text{preheating}}). \tag{35}$$

Due to the symmetry conditions on the sides (see Fig. 15) and by using mass conservation in steady-state, one can write:

$$\dot{M}_{\text{in}} = \langle \dot{m}_n \rangle^{\mathcal{A}} \tag{36}$$

where $\langle \cdot \rangle^{\mathcal{A}}$ denotes surface integration on $\mathcal{A}$. Recalling the definition of Γ in Eq. (33), it comes that:

$$\Gamma = \Gamma_w \frac{\langle \dot{m}_n \rangle^{\mathcal{A}}}{\mathcal{A}\, \dot{m}_0}, \tag{37}$$

where the flame wrinkling factor Γ_w is introduced:

$$\Gamma_w = \frac{\mathcal{A}}{\overline{\epsilon}\, \mathcal{A}_T}. \tag{38}$$

Injecting Eq. (35) into Eq. (37) yields:

$$\Gamma = \Gamma_w \frac{\langle \Gamma_p(T_{\text{preheating}}) \rangle^{\mathcal{A}}}{\mathcal{A}}. \tag{39}$$

Equation (39) shows that, assuming locally-adiabatic thin flame fronts, the global burning rate is given by the mean effect of preheating on $\mathcal{A}$, multiplied by the intensity of flame wrinkling. It is then insightful to consider the hypothesis of commutation of the surface integral with Γ_p, which boils down to the simple formula:

$$\Gamma = \Gamma_w \cdot \Gamma_p(\langle T_{\text{preheating}} \rangle^{\mathcal{A}}). \tag{40}$$

Equation (40) suggests that global burning rate is a simple product of the flame area and a mean preheating acceleration. Unfortunately, rigorously

$\langle T_{\text{preheating}} \rangle^{\mathcal{A}}$ does not necessarily correspond to the volume-averaged temperature $\langle T_g \rangle^g$, say, at the mean location or upstream of the flame fronts. Wrinkling and axial distribution make this quantity intrinsically non-unidimensional and somewhat uncorrelated to the volume averages. This limitation in mind, one may still approximate:

$$\Gamma = \Gamma_w \cdot \Gamma_p(\langle T_{\text{preheating}} \rangle^g), \tag{41}$$

where $\langle T_{\text{preheating}} \rangle^g$ is the preheating of the flame in the VAM.

5.2. Flamelet approach: phenomenology in the VAM

In previous theoretical works on the volume-averaged equations [22, 45], the authors have suggested the existence of a combustion regime where the flame front is locally adiabatic. It is named *decoupled*, and corresponds typically to low values of h_V. In this regime, flame acceleration is governed by preheating and the resulting burning rate is:

$$\Gamma = \Gamma_p(\langle T_{\text{preheating}} \rangle^g). \tag{42}$$

However, Eq. (42) does not take into account the additional flame acceleration related to dispersion. Assuming that the "dispersed" flame remains in the decoupled regime, an estimation of the burning rate in the VAM is:

$$\Gamma = \Gamma_d \cdot \Gamma_p(\langle T_{\text{preheating}} \rangle^g), \tag{43}$$

where Γ_d represents the flame acceleration due to dispersion. Recalling the asymptotic result that flame speed varies like the square root of thermal diffusivity [33], an approximate expression for Γ_d may be obtained:

$$\Gamma_d = \left(\frac{\langle \lambda_g \rangle^g + \langle \rho_g \rangle^g \left\langle c_{p_g} \right\rangle^g D^{\text{dis}}}{\langle \lambda_g \rangle^g} \right)^{1/2}. \tag{44}$$

In practice Γ_d varies a bit throughout the flame front, but to have an idea of its magnitude, its value in the fresh gases is given in Tab. 6.

5.3. Correction for the reaction rates

The analyses from Sec. 5.1 and Sec. 5.2 show two different expressions for Γ through Eq. (41) and Eq. (43). Assuming Eq. (41) suitable in the presence of thin flame fronts, it suggests that Γ should be multiplied by Γ_w/Γ_d

in the VAM. This makes sense because it includes flame acceleration caused by wrinkling whilst removing that from macroscopic dispersion (which, following the present analysis, should be unrelated to the microscopic burning rates). To achieve this, one may consider another result of asymptotic theory which states that burning rate is proportional to the square root of the pre-exponential factors, and write:

$$\langle \dot{\omega}_k \rangle^g = \left[\frac{\Gamma_w}{\Gamma_d} \right]^2 \cdot \dot{\omega}_k \left(\langle \rho_g \rangle^g , \langle T_g \rangle^g , \langle Y_k \rangle^g \right). \tag{45}$$

In the authors' knowledge, Eq. (45) constitutes the first attempt at correcting the macroscopic reaction rates in VAM for PMC.

5.4. Estimation of the flame surface in the DPLS

Equation (45) requires a value for flame surface. But because real flame fronts are not infinitely-thin, this quantity is not easy to estimate. Even when the flames are relatively thin compared to the pore size, they remain of finite width and affected by the proximity of the porous walls and distorted in the interstitial flow. Accordingly, the choice of a relevant flame surface deserves some discussion. Fig. 16 shows slices of heat release rate in various domains, along with two iso-surfaces of fuel progress variable $c = 1\%$ and $c = 80\%$, defined by:

$$c = 1 - \frac{Y_{\mathrm{CH4}}}{Y_{\mathrm{CH4,in}}}. \tag{46}$$

From Fig. 16, one may argue that $c = 80\%$ is a good definition of the flame surface, nearing regions of maximum heat release rate. Nevertheless, following Fig. 15 and the rationale of Sec. 5.1, the flame surface should also capture the information of local preheating, a quantity which is impossible to evaluate at $c = 80\%$ due to the heat released by combustion. As such, one may consider instead the surface $c = 1\%$ ahead of reaction and diffusion zones. Unfortunately, due to the distortion and axial distribution of the flame pockets, this surface does not appear satisfactory either. This issue is similar to the questions arising in turbulent combustion to which iso-c is the relevant flame surface, with the additional difficulty of non-homogeneous preheating and the presence of hot walls. Table 6 provides values of Γ_w obtained by considering either $c = 1\%$ or $c = 80\%$ as well as their relative difference. It is observed that the surface at $c = 1\%$ is systematically lower than that at $c = 80\%$, especially for the large pore case D4 due to the presence of very

distorted flame fingers (see Fig. 16). Also, it seems that Γ_w decreases with pore size. In the absence of a simple and definite answer to this question, it is chosen to stick to the surface $c = 80\%$ to feed Eq. (45).

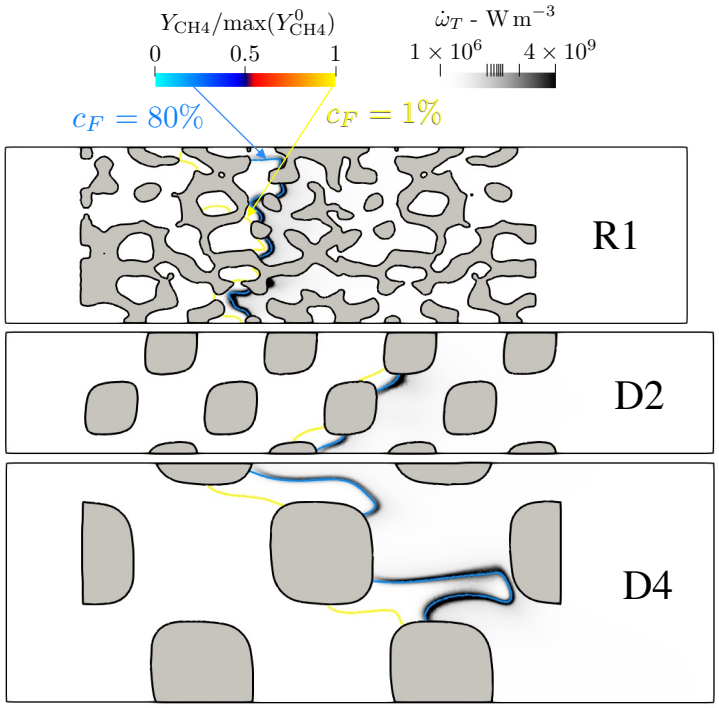

Figure 16: Isocontours of 1% and 80% of fuel consumption (progress variable c).

Table 6: Γ, Γ_w and Γ_d values.

	R2	R1	D4	D2	D1
Γ_w with surface $c = 1\%$	1.39	1.47	2.54	1.49	1.34
Γ_w with surface $c = 80\%$	1.69	1.63	3.83	1.80	1.38
relative diff. Γ_w ($c = 1 \rightarrow 80\%$)	+21%	+10%	+50%	+21%	+3%
Γ_d (fresh gases)	7.25	5.67	5.72	3.76	2.84

5.5. An acceleration related to macroscopic dispersion?

Considering the values of Γ_d and Γ_w in Tab. 6, it seems that the accelerations related to dispersion and the increase in flame surface have different

magnitudes and appear uncorrelated. This seems to show again that dispersion is not a good model to describe the pore-level combustion processes. This is consistent with the view of localized thin flame fronts which may not "see" dispersion at their scale. This reasoning may be further substantiated by considering the limit $h_V \to 0$. In that case Equation (16) becomes that of an adiabatic flame of increased thermal conductivity. In adiabatic porous burners, the flame acceleration was shown to be only related to the flame surface [13], which has no reason to be quantitatively linked to the magnitude of dispersion. Here for instance between cases R2 and D2, the flame areas are basically the same in the DPLS but intensities of dispersion are very different which is a source of error on Γ in the VAM.

5.6. Flamelet approach: VAM results

VAM simulations are performed using Eq. (45), and the resulting Γ values are reported in Fig. 17. The largest discrepancies are observed for R topologies. In order to assess more precisely the respective performance of Eq. (45) and Eq. (22), Fig. 18 provides their relative difference in terms of Γ values compared to the DPLS. The proposed Eq. (45) has errors of the same order than Eq. (22), keeping in mind that the good performance of Eq. (45) for D2 and D1 likely originates from error cancellation. The most salient feature of Fig. 17 is that the proposed closure for the reaction rates has a tendency to underestimate burning rate. Nonetheless, compared to the original closure, the error seems to be less erratic/random. This is attributed to the consideration of internal flame surface and the tempering of the influence of dispersion, and to that regard it may be viewed as an improvement.

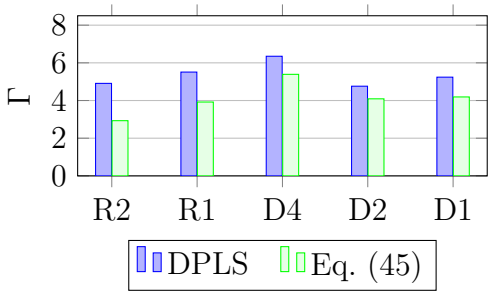

Figure 17: Performance of the new closure reaction rates.

Predictions for temperatures and heat release rate profiles using Eq. (45) are provided in App. C (see Supplementary Material). They show only limited improvement of temperature predictions.

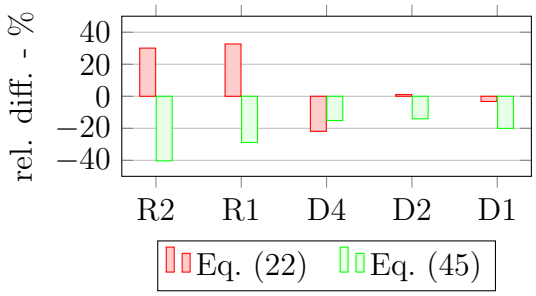

Figure 18: Relative performance of Eq. (22) and Eq. (45) compared to the DPLS in terms of Γ values.

5.7. Sources of errors in the flamelet approach

We conclude this work by considering more precisely the sources of error associated to the flamelet approach, which assumes that the flame fronts are locally adiabatic both in the DPLS and the VAM.

DPLS: in order to check if the flame front is locally adiabatic and only subject to preheating effects, one may assess whether Eq. (35) holds in the DPLS. Because Eq. (35) requires the information of preheating it is relevant to consider the surface $c = 1\%$, bearing in mind the associated difficulties addressed in Sec. 5.4. In order to study the local influence of the interstitial flow on burning rate, it is chosen to compute stretch rate κ on that surface, defined in steady-state by:

$$\kappa = \nabla_t \cdot \mathbf{u_t}, \tag{47}$$

where the tangential component of velocity $\mathbf{u_t}$ and divergence operator ∇_t on $\mathcal{A}$ are [33]:

$$\mathbf{u_t} = \mathbf{u} - (\mathbf{u}\cdot\mathbf{n})\mathbf{n} \qquad \text{and} \qquad \nabla_t \cdot \mathbf{u_t} = -\mathbf{nn} : \nabla\mathbf{u_t} + \nabla\cdot\mathbf{u_t}. \tag{48}$$

The influence of stretch on Eq. (35) is exemplified for case D2 through the scatter plot of $\dot{m}_n/\dot{m}_0\Gamma_p(T_{\text{preheating}})$ *vs.* reduced stretch rate $\kappa\delta_L^0/S_L^0$ given in Fig. 19. Joint probability densities are also drawn on the sides. Blue points indicate colder regions at the center of the pores, red points hotter regions near the walls. The black cross in the middle marks the mean values. Additionally, a fit with a function of the form $1 + c\cdot\kappa\,\delta_L^0/S_L^0$ is added in Fig. 19, underpinning a preheated-stretched flamelet hypothesis:

$$\dot{m}_n = \dot{m}_0\ \Gamma_p(T_{\text{preheating}})\left[1 + c\cdot\kappa\frac{\delta_L^0}{S_L^0}\right]. \tag{49}$$

Overall, three important conclusions may be drawn from Fig. 19:

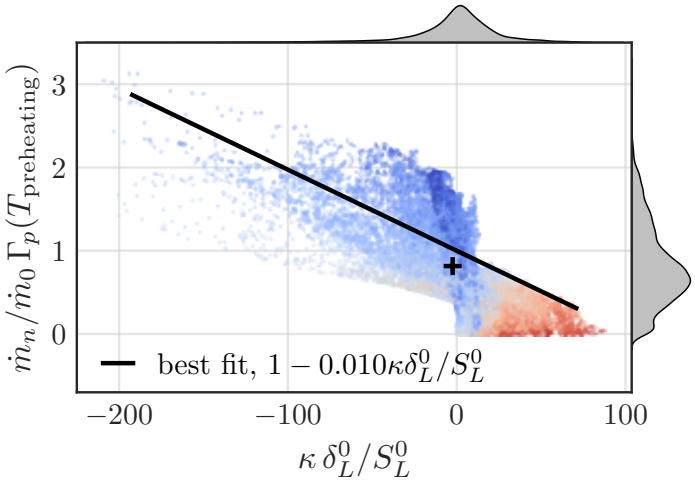

Figure 19: Scatter of local mass flux per surface unit, reduced by the corresponding preheated 1D mass flux versus reduced stretch. Associated PDFs on the sides. Domain D2. Blue points corresponds to cold regions (pore centers), red points to hot regions (near the walls).

- the mean value of $\dot{m}_n/\dot{m}_0\Gamma_p(T_{\text{preheating}})$ is 0.81, implying that on average, the 1D adiabatic-preheated flamelet hypothesis of Eq. (35) is valid at 81% on case D2;
- due to the no-slip conditions at the wall, there is a boundary layer for which $\dot{m}_n \to 0$ (red points). This may explain below-unity value for the mean value of $\dot{m}_n/\dot{m}_0\Gamma_p(T_{\text{preheating}})$. It corresponds to the quenching of the flame near the walls;
- although large positive stretch is found near the walls (flame feet) and large negative stretch is found at the core of the pore (flame tips), the average effect on the burning rate is negligible, as shows the cross centered near zero stretch.

Similar trends are found for all geometries, though due to the stochastic nature of the reticulated geometries more noise is visible (see App. D in Supplementary material, case R2).

VAM: in previous works from the authors [45], it was proven that the flame front can be considered locally adiabatic in the so-called *decoupled* regime, which is defined via two reduced parameters $r_{\dot{m}}$ and r_λ (see [45] for definitions). Fig. 20 shows the location of the different cases in the space ($r_{\dot{m}}$, r_λ) with the limits of the different regimes. Because in [45] dispersion was not intrinsically included, black points represent solutions without dispersion and grey points solutions with dispersion included under the form of an augmentation of the gas thermal conductivity (value computed in the fresh gases). It is observed that depending on the definition of $r_{\dot{m}}$ and r_λ, it is possible to classify the solutions either inside or outside of the decoupled regime. Nonetheless, in the intermediate regime, the burning rate remains partly governed by preheating so overall one can consider that the methodology for the present cases is valid at the leading order and in terms of phenomenology.

Other sources of errors and discussion: the above reasoning and comments upon the values of Γ suffer from many additional sources of error which may explain the differences in terms of profiles and Γ values. For example, it was observed in the cuts of Fig. 10 that the length scale of flame cooling is tendentially smaller than that of preheating, which is consistent with the underestimation of interphase heat transfer in Fig. 8. This reduction in cooling distance increases the temperature of the solid in the DPLS (see Fig. 12), which in turn increases Γ and is coherent with the trend observed in Fig. 17.

Other sources of error include the axial variations in ϵ, not included in the modelling; errors in the estimation of effective properties; and the fact that their intensity and functional form is not exactly the same between independent and coupled simulations. Overall, one should remember that current VAM frameworks are not derived rigorously from the microscopic equations. This is a large issue because the aggregation of macroscopic models for convection, diffusion, interphase heat exchange and highly non-linear exothermic reactions presents a phenomenology *a priori* uncorrelated to local combustion processes. This is particularly well illustrated by the cases R1 and D1 which have same Γ value in the DPLS for same flame position, but not in the VAM fed by different intensities of dispersion.

Albeit not radically improving predictions in terms of Γ values, the proposed modelling strategy for the reaction rates is based on a more rigorous theoretical and phenomenological approach. Unfortunately, it requires the estimation of the internal flame surface which is for now evaluated *a posteri-*

ori. It may be a simple function of the pore diameter but more simulations are required to confirm the trend and propose an accurate correlation to be used *a priori*. The authors believe relevant to test Eq. (45) in future experimental and numerical works, bearing in mind that it is was built in the framework of pore sizes larger than flame thickness. Note that the axial distribution of flame pockets has not been addressed and the authors did not find a way to include it in the VAM.

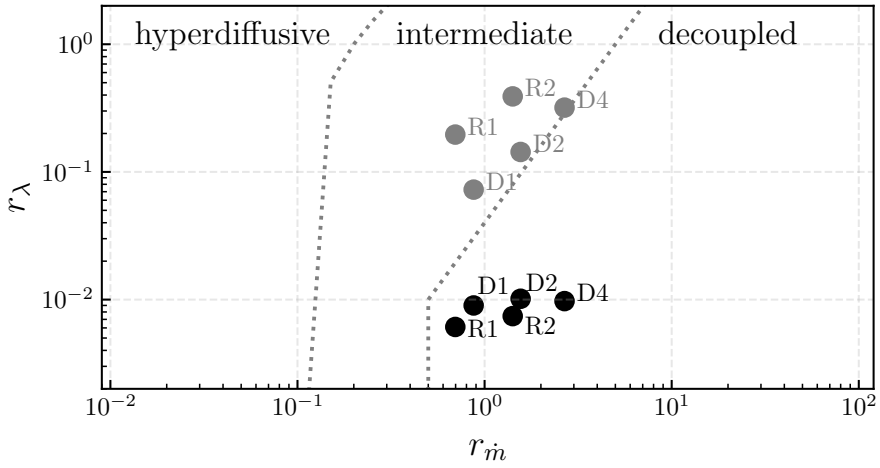

Figure 20: Localization of the cases considered wrt. the combustion regimes theorized in [45]. See the afferent article for notations and definitions. Black points: without dispersion. Grey points: with dispersion.

6. Conclusions

3D direct numerical simulations of methane-air combustion in porous burners of finite length were conducted for various pore sizes and geometries, in cases where the flame thickness is lower than the mean pore size and for steady-state conditions. A corresponding volume-averaged model based on classical equations and the same thermo-chemical scheme was fed with effective properties estimated directly on the computational domains. Direct comparisons between the 3D simulations and the 1D filtered model in terms of burning rate, physical profiles and *a priori* analysis could be achieved accordingly. This led to the following conclusions:

- in the 3D DPLS, sharp, wrinkled and longitudinally-distributed flame fronts are observed, in apparent contradiction with the upscaling hypotheses of the volume-averaged model. More especially, for 4 mm pores it is found that the flame fronts can be distorted across several pores;

- substantial discrepancies in terms of burning rate and spatially-averaged profiles are observed between the VAM predictions and the DPLS;

- an *a priori* analysis on heat release rate shows that the commutation assumption of reaction rates with their volume average is largely incorrect;

- the longitudinal distribution of the flame fronts along the burner axis makes the spatially-averaged profiles broader than in the VAM, which model a unique flame front;

- hydrodynamic dispersion does not seem to drive directly the burning rate of the flames at pore scale in the DPLS, contrary to the VAM where the increase in diffusivities systematically enhances flame speeds. It was attempted to solve this phenomenological contradiction by a modification of the reaction rates, but the proposed model seems to underpredict burning rates;

- locally, the burning rate of the flame fronts seems to be governed by a combination of preheating and wall quenching, while stretch effects seem to have negligible influence on average. However, the local non-adiabaticity related to this wall quenching are not modelled at the macroscale to date.

Possible work directions include the consideration of unsteady cases, different geometries/fuels, and the inclusion of radiation in both the DPLS and VAM.

8. Acknowledgements

This project was funded by ERC Horizon 2020 research and innovation program Grant Agreement 832248, SCIROCCO.

The HPC resources of BSC (PRACE project GASTON) and IDRIS (allocation A0112B10627 by GENCI) are acknowledged.

References

[1] J. L. Ellzey, E. L. Belmont, C. H. Smith, Heat recirculating reactors: Fundamental research and applications, Prog. Energ. Combust. 72 (2019) 32–58.

[2] F. Weinberg, Combustion temperatures: the future?, Nature 233 (1971) 239–241.

[3] M. Sahraoui, M. Kaviany, Direct simulation vs volume-averaged treatment of adiabatic, premixed flame in a porous medium, Int. J. Heat Mass Tran. 37 (1994) 2817–2834.

[4] J. Howell, M. Hall, J. Ellzey, Combustion of hydrocarbon fuels within porous inert media, Prog. Energ. Combust. 22 (1996) 121 – 145.

[5] J. Dunnmon, S. Sobhani, M. Wu, R. Fahrig, M. Ihme, An investigation of internal flame structure in porous media combustion via X-ray Computed Tomography, Proc. Combust. Inst. 36 (2017) 4399–4408.

[6] R. V. Fursenko, I. A. Yakovlev, E. S. Odintsov, S. D. Zambalov, S. S. Minaev, Pore-scale flame dynamics in a one-layer porous burner, Combust. Flame (2021) 111711.

[7] J. Kiefer, M. Weikl, T. Seeger, F. Von Issendorff, F. Beyrau, A. Leipertz, Non-intrusive gas-phase temperature measurements inside a porous burner using dual-pump CARS, Proc. Combust. Inst. 32 (2009) 3123–3129.

[8] M. Weikl, S. Tedder, T. Seeger, A. Leipertz, Investigation of porous media combustion by coherent anti-stokes raman spectroscopy, Experiments in fluids 49 (2010) 775–781.

[9] B. Stelzner, C. Keramiotis, S. Voss, M. Founti, D. Trimis, Analysis of the flame structure for lean methane–air combustion in porous inert media by resolving the hydroxyl radical, Proc. Combust. Inst. 35 (2015) 3381–3388.

[10] G. Brenner, K. Pickenäcker, O. Pickenäcker, D. Trimis, K. Wawrzinek, T. Weber, Numerical and experimental investigation of matrix-stabilized methane/air combustion in porous inert media, Combust. Flame 123 (2000) 201–213.

[11] R. Francisco Jr, F. Rua, M. Costa, R. Catapan, A. Oliveira, Combustion characteristics of gaseous fuels with low calorific value in a porous burner, in: Proceedings of the European Combustion Meeting, Citeseer, 2009.

[12] C. Hackert, J. Ellzey, O. Ezekoye, Combustion and heat transfer in model two-dimensional porous burners, Combust. Flame 116 (1999) 177–191.

[13] J. C. Ferguson, S. Sobhani, M. Ihme, Pore-resolved simulations of porous media combustion with conjugate heat transfer, Proc. Combust. Inst. 38 (2021) 2127–2134.

[14] F. Sirotkin, R. Fursenko, S. Kumar, S. Minaev, Flame anchoring regime of filtrational gas combustion: Theory and experiment, Proc. Combust. Inst. 36 (2017) 4383–4389.

[15] Y. Liu, Y. Deng, J. Shi, R. Xiao, H. Li, Pore-level numerical simulation of methane-air combustion in a simplified two-layer porous burner, Chin. J. Chem. Eng. 34 (2021) 87–96.

[16] C. Bedoya, I. Dinkov, P. Habisreuther, N. Zarzalis, H. Bockhorn, P. Parthasarathy, Experimental study, 1D volume-averaged calculations and 3D direct pore level simulations of the flame stabilization in porous inert media at elevated pressure, Combust. Flame 162 (2015) 3740–3754.

[17] P.-L. Billerot, L. Dufresne, R. Lemaire, P. Seers, 3D CFD analysis of a diamond lattice-based porous burner, Energy 207 (2020) 118160.

[18] I. Yakovlev, S. Zambalov, Three-dimensional pore-scale numerical simulation of methane-air combustion in inert porous media under the conditions of upstream and downstream combustion wave propagation through the media, Combust. Flame 209 (2019) 74–98.

[19] J. Shi, J. Lv, F. Behrendt, Y. Liu, M. Mao, F. He, 3D pore-scale simulations and 1D volume-averaged calculations of the flow and thermal non-equilibrium for low-velocity filtration combustion, Int. J. Heat Mass Tran. 177 (2021) 121532.

[20] S. Zhdanok, L. A. Kennedy, G. Koester, Superadiabatic combustion of methane air mixtures under filtration in a packed bed, Combust. Flame 100 (1995) 221–231.

[21] I. Yakovlev, A. Maznoy, S. Zambalov, Pore-scale study of complex flame stabilization phenomena in thin-layered radial porous burner, Combust. Flame 231 (2021) 111468.

[22] P.-A. Masset, O. Dounia, L. Selle, Fully explicit formulae for flame speed in infinite and finite porous media, Combust. Theory Model. (2021) 1–28.

[23] S. B. Sathe, R. E. PECK, T. W. Tong, Flame stabilization and multimode heat transfer in inert porous media: a numerical study, Combust. Sci. Technol. 70 (1990) 93–109.

[24] M. Quintard, S. Whitaker, Transport in ordered and disordered porous media ii: Generalized volume averaging, Transport in porous media 14 (1994) 179–206.

[25] M. Sahraoui, M. Kaviany, Direct simulation vs volume-averaged treatment of adiabatic, premixed flame in a porous medium, Int. J. Heat Mass Transf. 37 (1994) 2817 – 2834.

[26] K. Yamamoto, N. Takada, M. Misawa, Combustion simulation with lattice boltzmann method in a three-dimensional porous structure, Proc. Combust. Inst. 30 (2005) 1509–1515.

[27] N. Jouybari, M. Maerefat, M. Nimvari, A pore scale study on turbulent combustion in porous media, Heat Mass Transfer 52 (2016) 269–280.

[28] A. G. Dixon, Local transport and reaction rates in a fixed bed reactor tube: Endothermic steam methane reforming, Chem. Eng. Sci. 168 (2017) 156–177.

[29] N. Djordjevic, P. Habisreuther, N. Zarzalis, Numerical simulation of the combustion in porous media: relative importance of the different transport mechanisms for the flame stabilization, in: Proc. 6th Mediterranean Combustion Symposium, 2009.

[30] S. Sobhani, P. Muhunthan, E. Boigné, D. Mohaddes, M. Ihme, Experimental feasibility of tailored porous media burners enabled via additive manufacturing, Proc. Combust. Inst. 38 (2021) 6713–6722.

[31] O. Colin, M. Rudgyard, Development of high-order Taylor–Galerkin schemes for LES, J. Comput. Phys. 162 (2000) 338–371.

[32] T. J. Poinsot, S. K. Lele, Boundary conditions for direct simulations of compressible viscous flows, J. Comput. Phys. 101 (1992) 104–129.

[33] T. Poinsot, D. Veynante, Theoretical and numerical combustion, RT Edwards, Inc., 2005.

[34] E. Ranzi, A. Frassoldati, R. Grana, A. Cuoci, T. Faravelli, A. P. Kelley, C. K. Law, Hierarchical and comparative kinetic modeling of laminar flame speeds of hydrocarbon and oxygenated fuels, Prog. Energ. Combust. 38 (2012) 468–501.

[35] Q. Cazères, P. Pepiot, E. Riber, B. Cuenot, A fully automatic procedure for the analytical reduction of chemical kinetics mechanisms for Computational Fluid Dynamics applications, Fuel (2021).

[36] P. Pepiot-Desjardins, H. Pitsch, An efficient error-propagation-based reduction method for large chemical kinetic mechanisms, Combust. Flame (2008).

[37] T. Lu, C. K. Law, Systematic approach to obtain analytic solutions of quasi steady state species in reduced mechanisms, J. Phys. Chem. A (2006).

[38] F. Duchaine, S. Jauré, D. Poitou, E. Quémerais, G. Staffelbach, T. Morel, L. Gicquel, Analysis of high performance conjugate heat transfer with the OpenPalm coupler, Comput. Sci. Discov. 8 (2015) 015003.

[39] V. Frayssé, L. Giraud, S. Gratton, A set of GMRES routines for real and complex arithmetic on high performance computers, CERFACS (2003).

[40] I. Malico, J. C. F. Pereira, Numerical study on the influence of radiative properties in porous media combustion, J. Heat Transfer 123 (2001) 951–957.

[41] D. Diamantis, E. Mastorakos, D. Goussis, Simulations of premixed combustion in porous media, Combust. Theory Model. 6 (2002) 383.

[42] A. J. Barra, J. L. Ellzey, Heat recirculation and heat transfer in porous burners, Combust. Flame 137 (2004) 230–241.

[43] M. Mendes, J. Pereira, J. Pereira, A numerical study of the stability of one-dimensional laminar premixed flames in inert porous media, Combust. Flame 153 (2008) 525–539.

[44] F. Duchaine, N. Maheu, V. Moureau, G. Balarac, S. Moreau, Large-eddy simulation and conjugate heat transfer around a low-mach turbine blade, J. Turbomach. 136 (2014) 051015.

[45] P.-A. Masset, O. Dounia, L. Selle, Combustion regimes in inert porous media: From decoupled to hyperdiffusive flames, Combust. Flame 241 (2022) 112052.

[46] D. G. Goodwin, H. K. Moffat, R. L. Speth, Cantera: An object-oriented software toolkit for chemical kinetics, thermodynamics, and transport processes, 2017. Version 2.3.0.

[47] F. Kuwahara, M. Shirota, A. Nakayama, A numerical study of interfacial convective heat transfer coefficient in two-energy equation model for convection in porous media, Int. J. Heat Mass Transf. 44 (2001) 1153–1159.

[48] N. Wakao, S. Kaguei, Heat and mass transfer in packed beds, gorden and breach sci, Publishers, New York (1982) 243–295.

[49] A. Zukauskas, Heat transfer from tubes in crossflow, in: Advances in heat transfer, volume 8, Elsevier, 1972, pp. 93–160.

[50] M. B. Saito, M. J. S. de Lemos, A Correlation for Interfacial Heat Transfer Coefficient for Turbulent Flow Over an Array of Square Rods, Journal of Heat Transfer 128 (2005) 444–452.

[51] V. N. Kurdyumov, D. Fernández-Galisteo, C. Jiménez, Asymptotic study of premixed flames in inert porous media layers of finite width: Parametric analysis of heat recirculation phenomena, Combust. Flame 241 (2022) 112109.

[52] J. Delgado, Longitudinal and transverse dispersion in porous media, Chem. Eng. Res. Des. 85 (2007) 1245–1252.